



UvA-DARE (Digital Academic Repository)

Glow with the flow: Quantifying blood flow and photoluminescence signal in biological tissue

Nadort, A.

Publication date

2015

Document Version

Final published version

[Link to publication](#)

Citation for published version (APA):

Nadort, A. (2015). *Glow with the flow: Quantifying blood flow and photoluminescence signal in biological tissue*. [Thesis, fully internal, Universiteit van Amsterdam].

General rights

It is not permitted to download or to forward/distribute the text or part of it without the consent of the author(s) and/or copyright holder(s), other than for strictly personal, individual use, unless the work is under an open content license (like Creative Commons).

Disclaimer/Complaints regulations

If you believe that digital publication of certain material infringes any of your rights or (privacy) interests, please let the Library know, stating your reasons. In case of a legitimate complaint, the Library will make the material inaccessible and/or remove it from the website. Please Ask the Library: <https://uba.uva.nl/en/contact>, or a letter to: Library of the University of Amsterdam, Secretariat, P.O. Box 19185, 1000 GD Amsterdam, The Netherlands. You will be contacted as soon as possible.



4

QUANTITATIVE BLOOD FLOW VELOCITY IMAGING
USING LASER SPECKLE FLOWMETRY

Adapted from:

A. Nadort, K. Kalkman, T. G. van Leeuwen, and D. J. Faber, "Quantitative blood flow velocity imaging using laser speckle flowmetry" (in submission).

4

ABSTRACT Laser speckle flowmetry suffers from a debated quantitative relationship with blood flow, velocity or tissue perfusion and a lack of calibration of the inverse relationship $1/\tau_c = \alpha V$ between decorrelation time (τ_c) and flow velocity (V). Using a modified microcirculation imager, we experimentally investigate on the influence of the optical properties of scatterers on α *in vitro* and *in vivo*. We found a good agreement to theoretical predictions based on the scattering phase function, within certain limits for scatterer size and multiple scattering. We present a practical model-based scaling factor to correct for multiple scattering in microcirculatory vessels. Our results show that laser speckle flowmetry offers a quantitative measure of flow velocity in addition to vessel morphology, providing the quantification of local blood flow, velocity and tissue perfusion for clinically relevant applications.

4.1 INTRODUCTION

Quantification of microcirculatory blood supply to tissues is of paramount importance for diagnosis, therapy planning and monitoring, e.g. of metabolic, vascular and critical diseases [1, 2]. Quantifying cerebral blood flow gives insight into brain metabolism [3], while visualizing angiogenic vasculature can aid in localizing tumours [4, 5] and monitoring their development and oxygen metabolism [6-8]. Important clinical microcirculation parameters are blood flow (volume of blood per unit time in the vasculature) and perfusion (volume of blood per volume tissue, per unit time). Both are intimately related to (local) blood flow velocity through the morphology of the vasculature itself (e.g. local vessel diameters and vessel density). Laser speckle flowmetry [9] has become a widely available vascular imaging tool with the potential to be used at the bedside or during operations due to its technological simplicity, and high spatial and temporal resolution [10-14]. Direct quantification of blood flow velocity through imaging has the additional advantage of acquiring vessel morphology, leading to the quantification of local blood flow and perfusion. However, a true quantitative representation of blood flow velocity by laser speckle flowmetry techniques was hindered by multiple scattering inside the vessels and lack of calibration of the flow velocity and speckle dynamics [15, 16], which are both addressed in the following pages. We present a practical guideline to quantitative blood flow velocity measurements through laser speckle contrast imaging (LSCI), thereby enabling the quantitative estimation of functional microcirculatory parameters real time and non-invasively.

LSCI provides a measure for blood flow by quantifying the decrease in speckle contrast as a result of ‘blurring’ of dynamic speckles within a finite camera exposure time [9, 17]. When scatterers, e.g. red blood cells (RBCs), move the speckle contrast K , defined as the ratio of the standard deviation (σ) to the mean ($\langle I \rangle$) of the pixel intensity, decreases with increasing ratio of the camera exposure time T and the characteristic timescale of the speckle dynamics τ_c [18, 19]. The interpretation of τ_c as a measure of blood flow, velocity or tissue is confounded [15, 20], but represents a clinically relevant question. We investigate on this matter and show that the parameter τ_c can be quantitatively related to blood flow velocity.

Contributing to this quest we recently integrated sidestream dark field (SDF) microscopy [21, 22] with LSCI [19]. SDF-LSCI enabled us to simultaneously obtain speckle decorrelation times and flow velocities in microcirculatory vessels or phantom flow channels. We have shown that in biological tissue the speckle pattern decorrelates due to both desired and undesired dynamics and a first correction of τ_c for decorrelation sources other than blood flow (such as muscle movements) is needed. We will further validate LSCI by investigating on the relationship between τ_c and flow velocity (V). Albeit that the relation is verified to be of the form $1/\tau_c = aV$ in flow phantom experiments, the exact value of the proportionality constant a is debated and has not been verified *in vivo* [16, 23]. Suggestions for a ranged from a dependence on system parameters [16, 24, 25] to a dependence on the optical properties of the scatterers [26] and dependence on multiple scattering [16, 26]. These predictions differ 1-2 orders of magnitude [23]. In spite of this controversy speckle flowmetry has shown great clinical potential for visualizing vasculature and measuring relative flow velocities [10-13, 27-30], however, to become a true quantitative tool the assessment of a beyond speculation is a necessity. In this work, we quantify the $1/\tau_c = aV$ relation-

ship *in vivo*, which was suggested to depend on scatterer size through the scatterer phase function [26] and multiple scattering through the number of dynamic scattering events [16, 26]. To this end we investigate on the influence of scatterer size and volume fraction on α , using an *in vitro* flow phantom and solutions of polystyrene spheres. We place our results in theoretical context taking into account the optical properties and experimental geometry, resulting in a practical relation $1/\tau_c = \alpha' A(N) \times V$ where α' is the proportionality constant for single scattering events and $A(N)$ scales for the average number of dynamic scattering events N . Applying this theoretical framework to chick embryo and human microcirculation beds demonstrates the feasibility of LSCI for quantitative mapping of blood flow velocities (V) *in vivo*. As a guideline for the reader a flow chart presenting the sequential steps, which will be described in this Chapter, is shown in Fig. 4.1.

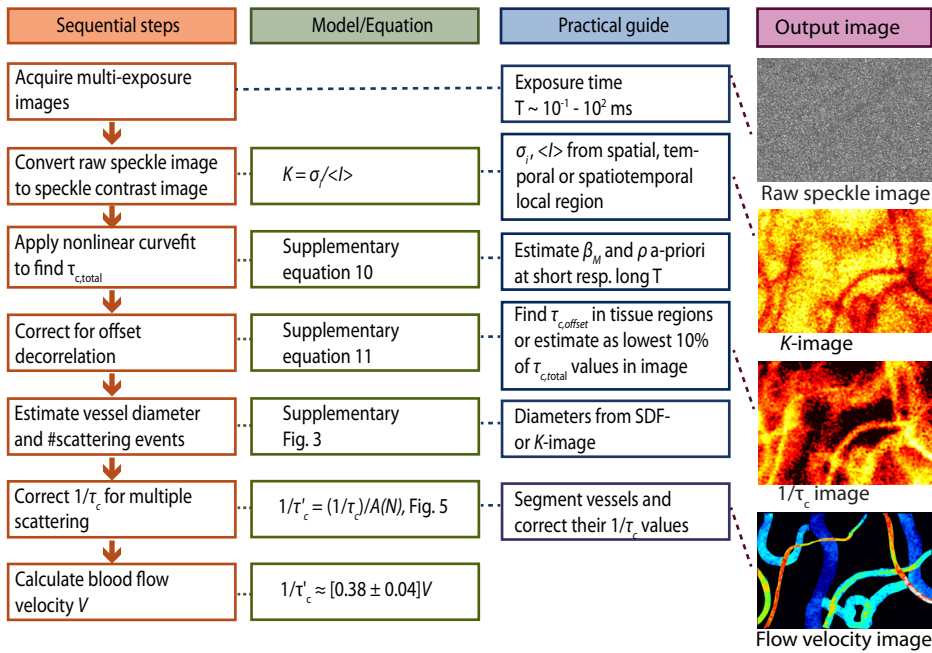


Figure 4.1 | Flow chart for quantitative laser speckle flowmetry. This paper discusses the sequential steps, theoretical model and practical guide to quantifying blood flow velocities *in vivo* using laser speckle contrast imaging (LSCI).

4.2 THEORETICAL FRAMEWORK

When coherent light backscattered from different positions in biological tissue is imaged on a camera, the ensemble of phase differences gives rise to a randomly varying spatial intensity distribution (speckle). Movement of scatterers results in a temporally fluctuating speckle pattern. The characteristic timescale τ_c of the fluctuation can be used to quantify the motion of scattering particles. However, τ_c also depends on optical and physical properties of the tissue, e.g. the scattering phase function and scattering from more than one moving particle causing faster decorrelation of the speckle pattern (shorter τ_c). We review the optical properties relevant to our application and their relationship with τ_c in

Supplementary section 4.1 a and 4.1b, respectively. The parameter τ_c parameterizes the temporal electric field autocorrelation function (ACF) $g_1(\tau)$ describing the sample dynamics. This approach builds upon the theoretical foundation of Laser Doppler Flowmetry (LDF) [26, 31], Diffusing Wave Spectroscopy (DWS) [32, 33] and using our recent advances in the modelling of optical scattering of whole blood [34]. Because for large concentrations of scatterers, as in blood, the scattering is not linear with their concentration, the inter-particle correlation (“dependent scattering”) has to be taken into account to estimate the real scattering coefficient. This correlation is implemented by modelling flowing blood as a discrete random medium of hard spheres which is characterized by the local density and pair correlation function. The latter is calculated using Percus-Yevick (PY) equations [35, 36] as before [34, 37]. Next the number of scattering events in the vessel has to be determined. The probability density for the number of scattering events per unit volume $p(n)$ is Poissonian only for low volume fractions of scatterers [26]. For RBCs in whole blood (volume fraction or hematocrit (Hct) 30 - 50%) we use a normal distribution for $p(n)$, where the relation between mean (N) and variance (σ_n^2) is determined by the pair correlation function [38, 39] (Supplementary section 4.1c). Here, N is estimated from Monte Carlo simulations of our measurement geometry (Supplementary section 4.2 and 4.3).

Temporal speckle dynamics can be derived from spatial intensity statistics of an imaged speckle pattern (Supplementary section 4.1d). After the initial derivation [9] essential improvements were included [40, 41], for example a correction for a static component in the speckle pattern. When a Gaussian form of $g_1(\tau)$ is appropriate [40] an analytical expression for speckle contrast $K(T/\tau_c)$ can be derived for curve fitting, where T is the camera exposure time. Next to the sought τ_c , the model incorporates the parameters β_M [19, 42, 43] (the measurement geometric calibration constant) and ρ (the fraction dynamically scattered light where $\rho = I_f / (I_f + I_s)$, with I_f the detected intensity of the fluctuating scattered light and I_s the detected intensity of the light scattered by static components) that can both be measured. The resulting expression is Supplementary Eq. (4.10), from which τ_c can be reliably estimated by applying a multi-exposure acquisition scheme and subsequent non-linear curve fit [28, 44].

4.3 METHODS

4.3.1 Data acquisition

To enable SDF-LSCI, a clinical microcirculation imager based on SDF microscopy (Microscan, Microvision Medical, The Netherlands) was modified to provide illumination with laser light (HeNe, 632.8 nm) guided through four optical multimode fibres surrounding a central imaging pathway with 5x magnification (Supplementary Fig. S4.1) [19], and an Airy disk of 4.2 μm . Light that is back reflected forms a speckle pattern on an 8-bit monochrome camera (IEEE 1394, Guppy F-080B, Allied Vision Technologies, Germany) with a field of view of 1 x 0.7 mm on 1024 x 768 pixels and 30 frames per second. The minimal speckle diameter was 2.2 pixels \approx 10.2 μm [45]. For conventional SDF imaging broad band green light (530 ± 20 nm) was coupled into the fibres to provide contrast between flowing RBCs and surrounding tissue to enable RBC flow measurement [46]. During *in vivo* data acquisition the SDF and SDF-LSCI modes were alternated to measure the flow velocity and decorrelation time of the same region [19].

4.3.2 *In vitro* flow phantom

We designed a tissue simulating flow phantom consisting of a polymer tube (diameter 0.2 ± 0.03 mm; depth 0.3 mm ± 0.03 mm, verified with OCT measurements [19]) embedded in silicone elastomer (Sylgard® 184 Silicone Elastomer DOW/Corning, US) mixed with titanium dioxide (TiO_2 , anatase form, Sigma Aldrich, US) in the concentration $[\text{TiO}_2] = 1$ mg/ml to mimic tissue scattering [47]. The tube was connected to a 0.5 ml syringe, slowly pressed by a syringe pump (Harvard model PHD2000, US) which resulted in a flow range of 0.1 - 20 mm/s. The flowing media consisted of polystyrene spheres with diameters $D = 0.6, 1, 2, 5, 7$ and $10 \mu\text{m}$ (Kisker-Biotech, Germany) with stock volume fraction of 2.5 vol%. For 1, 2 and $5 \mu\text{m}$ particles we prepared different volume fractions in the range 0.6 - 7 vol%. The range of scattering coefficients μ_s as calculated using Mie and Percus-Yevick theory [37] was 7 - 150 mm^{-1} as specified in Supplementary table S4.2. A complete flow series was repeated 2 or 3 times per sample, however, we note that for large spheres the low flows (< 1 mm/s) were excluded due to precipitation of scatterers.

4.3.3 *In vivo* microcirculation

We recorded multimodal *in vivo* SDF-LSCI image frames from the readily accessible microcirculation of a chick embryo at embryonic day 9, grown *ex ovo* [48]. The imaging tip of the integrated SDF-LSCI device was gently put in contact with the chorioallantoic membrane tissue to prevent disruption of blood flow. The human sublingual microcirculation SDF-LSCI dataset was previously obtained [19] and analyzed using the current model. For the sublingual microcirculation the device was hand-held, while it was secured in a stand for chick embryo microcirculation imaging.

4.3.4 Data analysis

In vitro: Speckle contrast K was calculated from the raw speckle images according to Supplementary Section S4.1d, Eq. (4.8) over a local region of 10×10 pixels. To obtain a multi-exposure curve, we applied an exposure time range of 0.3 - 30 ms using neutral density filters to prevent overexposure (Supplementary Fig. S4.4). For each T minimally 200 K -values were selected in the centre of the tube (standard deviation in $K < 5\%$). β_M and ρ were a-priori estimated at $T \ll \tau_c$ (static phantom) and at $T \gg \tau_c$ (flow > 15 mm/s and $T > 10$ ms) respectively, leaving τ_c the only fit parameter in Supplementary Eq. (4.10). Specifically, ρ was individually estimated for each scatterer size and volume fraction and kept constant for all other flow velocities in the same size/volume fraction series, while β_M is expected to be constant and was found to be 0.40 ± 0.02 . The goodness of nonlinear fit $\langle R_{\text{adj}}^2 \rangle$ averaged over all fits of $K(T)$ vs. T was 0.98 ± 0.02 .

In vivo: To calculate K a spatiotemporal local region of $7 \times 7 \times 20$ pixels was applied to optimize the *in vivo* spatiotemporal resolution and minimize the uncertainty in K [19], and minimally 25 K values were obtained per vessel and T (standard deviation in $K < 7\%$). The exposure time range was extended to longer T [0.5 - 100 ms] and ρ and β_M were a-priori estimated at long and short T respectively. In the subsequent curve fit both were constraint within 5% of their estimated value, and τ_c was unconstrained. The goodness of nonlinear fit $\langle R_{\text{adj}}^2 \rangle$ averaged over all fits was 0.99 ± 0.01 . The *in vivo* decorrelation times ($\tau_{c,\text{total}}$) were corrected for statistically independent sources of decorrelation (flow and muscle movement) via the 'offset' $\tau_{c,\text{offset}}$ measured from adjacent tissue as described in Supplementary

Eq. (4.11) [19]. Absolute flow measurements (maximal measurable flow < 2 mm/s) were obtained from videos acquired in conventional SDF-mode using commercially available software (AVA3.0, Microvision Medical, The Netherlands) [46]. To correct the decorrelation times for multiple scattering the number of scattering events N in the vessel were estimated using Monte Carlo simulations as described in Supplementary Section 4.3. Next, we calculated an *in vivo* scaling factor $A(N) = a(N)/a'$, where $a(N)$ was theoretically derived using the optical properties of blood (Supplementary table S4.1) for N scattering events, and a' for single scattering. Finally, $1/\tau_c$ was rescaled according to $1/\tau'_c = (1/\tau_c)/A(N)$.

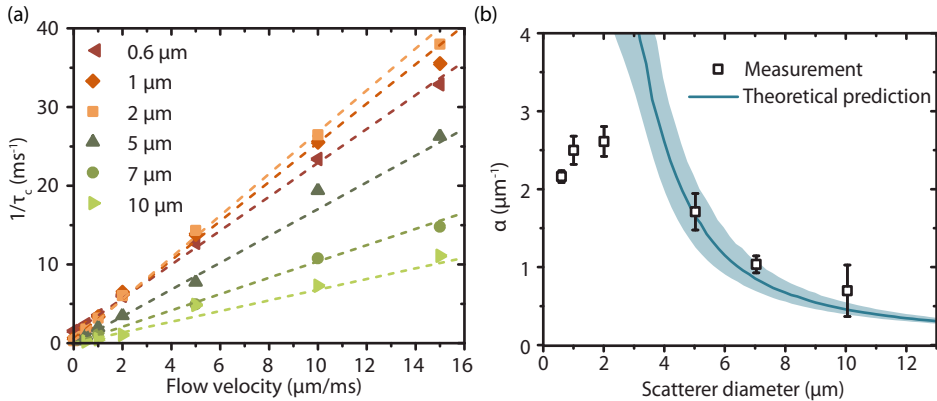


Figure 4.2 | Influence of size on α . (a) $1/\tau_c$ plotted against V for 6 different diameters of scatterers (polystyrene microspheres [0.6 - 10 μm]), together with a linear fit (dotted lines) to the data points with weights τ_c . The slope of the linear fit is α . No error bars are plotted for clarity, the average standard error on τ_c was $4\% \pm 2\%$ (max. error 12%). (b) α versus scatterer diameter, error bars are 95% CI intervals from linear fit in (a). Also plotted is the theoretically derived α (solid line) using Mie-Percus-Yevick scattering approximations and the number of scattering events N in the flow tube (diameter $d = 0.2 \pm 0.03$ mm) as obtained from Monte Carlo simulations ($N = 1.2\mu/d$). The shaded area represents the uncertainty in α due to error margins in optical properties of the scatterers.

4.4 RESULTS

4.4.1 Influence of size and volume fraction of scatterers

Experimental LSCI data was acquired using an integrated SDF-LSCI device (Supplementary Fig. S4.1). Multi-exposure SDF-LSCI frames were recorded for 9 flow velocities [0.1 - 20 mm/s] and 6 differently sized microspheres [diameter $D = 0.6 - 10 \mu\text{m}$; all 2.5 vol%] and τ_c was estimated by fitting Supplementary Eq. (4.10) to the measured speckle contrast (a typical example is shown in Supplementary Fig. S4.4). In Fig. 4.2a, $1/\tau_c$ vs. V is plotted for the different sphere sizes, where the slope defines α . For large scatterers (5, 7 and 10 μm) α increases with decreasing size. For small scatterers (0.6, 1 and 2 μm) however, α is approximately constant. The theoretical predictions for α follow from Supplementary Section 4.1 using the optical and physical properties listed in Supplementary Table S4.2 and Monte Carlo simulations for this geometry. Fig. 4.2b shows α plotted (data points) for all scatterer sizes, together with predictions (solid line). The shaded area represents the uncertainty in the calculation due to variations in size and refractive index of the scatterers. In order to determine the effect of concentration, we prepared different volume fractions of solutions of 1, 2 and 5 μm spheres (Supplementary table S4.2) and determined α shown in Fig. 4.3a together with α from 2.5 vol% solutions of 0.6, 7 and 10 μm . In Fig.

4.3b the same data points are plotted as a function of optical properties, scattering coefficient μ_s and N , which results in a more uniform increase of a with increasing μ_s resp. N , until a remains constant. Fig. 4.3c shows measured values vs. prediction yielding good correspondence for small a (low μ_s and N), however for higher a theory overestimates the experimental measurement.

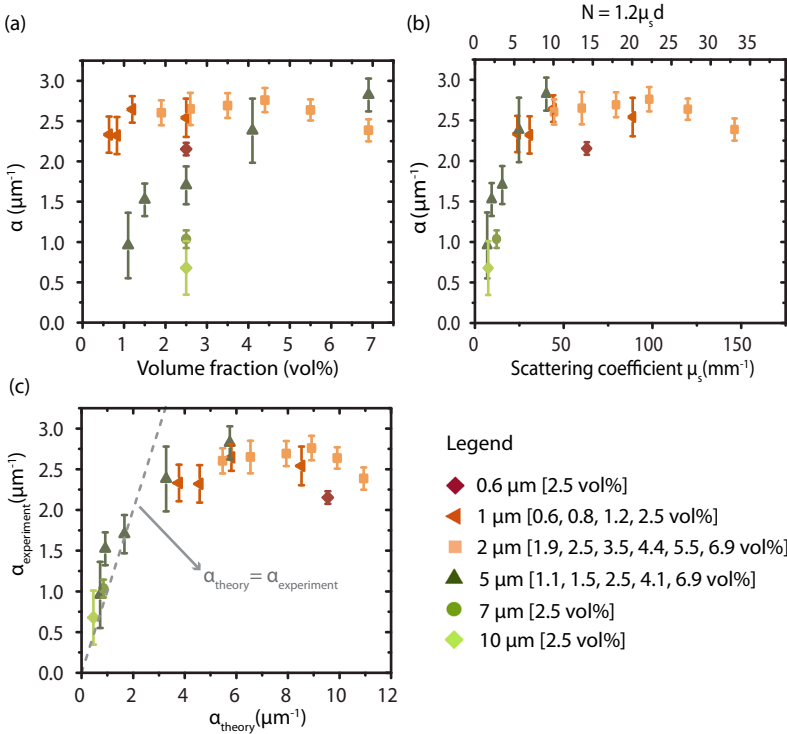


Figure 4.3 | Influence of volume fraction on α . Experimentally measured α versus (a) scatterer volume fraction, (b) scattering properties (μ_s and N in the flow tube with diameter $d = 0.2 \pm 0.03$ mm, $N = 1.2\mu_s d$) and (c) theoretically derived α for differently sized polystyrene spheres in varying volume fractions. Error bars are 95% CI intervals from linear fit on $1/\tau_c$ vs. V .

4.4.2 Quantitative flowmetry *in vivo*

We assessed *in vivo* decorrelation times by imaging the readily available microcirculation of the chorioallantoic membrane of a chick embryo grown *ex ovo*. Multi-exposure SDF-LSCI and conventional SDF frames were recorded for 35 unique vessels for which RBC tracking was possible, to independently estimate τ_c (by LSCI) and V (by SDF) of the same vessels. Compared to controlled phantom experiments, first it is essential to account for ‘offset’ decorrelation due to dynamic scattering of photons outside the focal plane [19]. Second, the average number of scattering events varies per vessel diameter, estimated from Monte Carlo simulations (Supplementary Section 4.3). Therefore, for each vessel a unique $\alpha(N, \mu_s, p(\mathbf{q}))$ can be found. We assume that for the microcirculation μ_s and $p(\mathbf{q})$ are invariant and we can write $\alpha(N)$. This allows rescaling of each τ_c to $N = 1$ by a model-based *in vivo* scaling factor $A(N) = \alpha(N)/\alpha'$, denoting the parameters rescaled for single

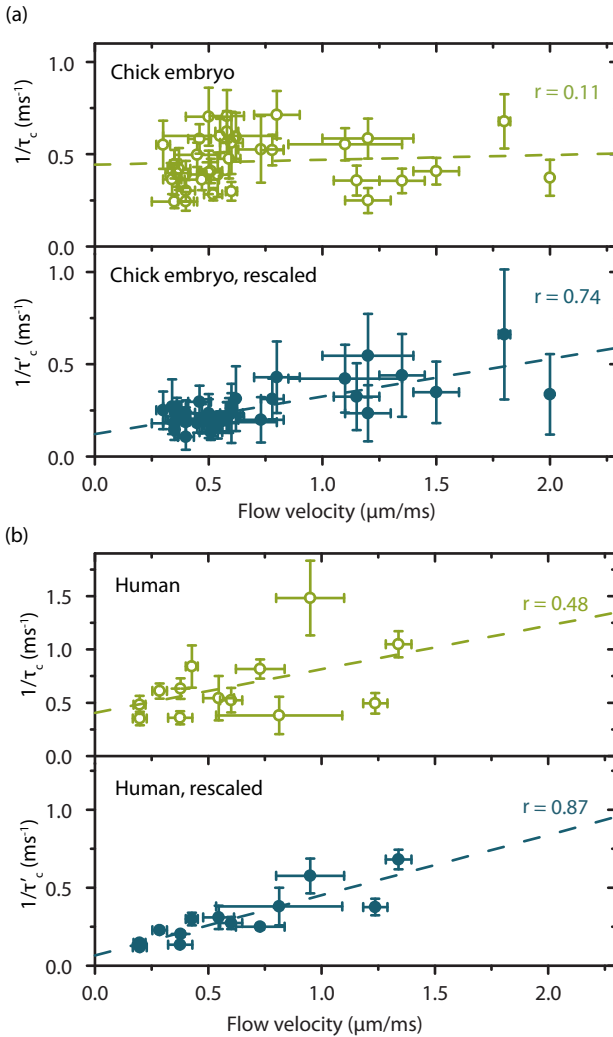
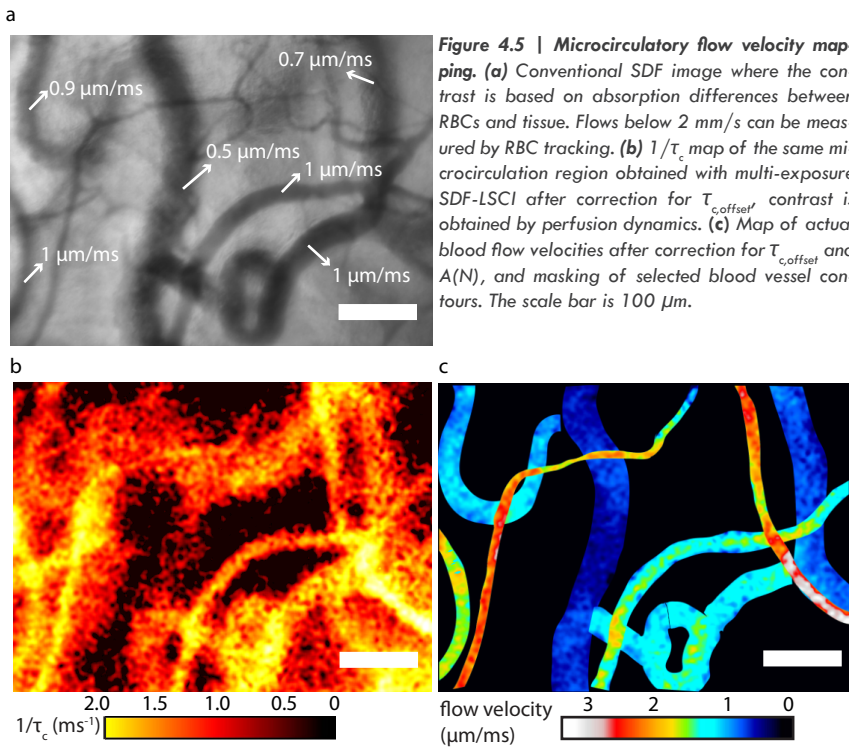


Figure 4.4 | In vivo determination of α' . $1/\tau_c$ versus V for RBCs in vivo, for (a) chick embryo and (b) human microcirculation. The top panels (green open circles) show $1/\tau_c$ estimated by a multi-exposure curve fit (Supplementary section Id, Eq. 4.10) and $\tau_{c,offset}$ correction (Supplementary Eq. (4.11) [19]). The bottom panels show $1/\tau'_c$ rescaled for multiple scattering (see text). In both (a) and (b) one data point was excluded as an outlier (not shown). Vertical error bars represent 95% CI of the multi-exposure curve fit and horizontal error bars represent the standard deviation in flow velocity measurements. The slope, or α' , is 0.20 ± 0.07 (95% CI) and 0.39 ± 0.15 for chick embryo respectively human RBCs, and the theoretical prediction for α' is 0.27 respectively 0.38.

scattering α' and τ'_c . In Fig. 4.4a $1/\tau_c$ (top panel) and $1/\tau'_c$ (bottom panel) are plotted versus blood flow velocity. The correlation coefficient of the linear fit of $1/\tau_c$ and $1/\tau'_c$ vs. V improved after rescaling from $r = 0.11$ to $r = 0.74$, respectively. The slope of the rescaled linear fit gave $\alpha' = 0.20 \pm 0.07$ (95% CI), close to theoretical $\alpha' = 0.27$ with an uncertainty range of $[0.24 - 0.30]$ calculated by varying the size $\pm 5\%$ and refractive index $n_{RBC} \pm 1\%$ (Supplementary table S4.1). The scaling factor $A(N)$ for chick embryo blood vessels is shown in Supplementary Fig. S4.5. Next, we reassessed the human sublingual microcirculation measurements acquired previously (14 unique vessels with known flow velocities) [19] by model-based rescaling of τ_c . The correlation coefficient increased from $r = 0.48$ to $r = 0.87$ between $1/\tau_c$ (Fig. 4.4b, top panel) and $1/\tau'_c$ data (Fig. 4.4b, bottom panel), respectively, vs. flow velocity. The *in vivo* α (human) was 0.41 ± 0.50 (95% CI) for the original data and α' was 0.39 ± 0.15 (95% CI) for the rescaled data, near identical to the

prediction for α' of 0.38 with an uncertainty range of [0.34 - 0.41] calculated by varying the size $\pm 5\%$ and $n_{RBC} \pm 1\%$. The quantity $1/\tau_c$ is essentially related to both flow velocity and vessel diameter, therefore a strong correlation with V is not expected, however, by correcting for volume fraction of RBCs the correlation is much improved as also evidenced by the reduction in 95% CI range for α' .

To illustrate the quantitative imaging ability of laser speckle flowmetry we constructed a $1/\tau_c$ map and a blood flow velocity map as shown in Fig. 4.5 and Supplementary Movie 1 (human) and Supplementary Movie 2 (chick embryo)[§], following the practical steps outlined in Fig. 4.1 and Supplementary Section 4.7. The scaling factor $A(N)$ for human blood vessels is shown in Fig. 4.6 for values of hematocrit corresponding to whole blood (Hct = 45 %) and the microcirculation (Hct = 30 %) [49].



4.5 DISCUSSION

In this Chapter we demonstrate non-invasive quantitative blood flow velocity measurements *in vivo*, using a relatively simple and available technique based on LSCI. LSCI suffers from a debated quantitative relationship with blood flow, velocity or tissue perfusion [15, 20]

[§] Movie 1 can be downloaded at

<https://www.dropbox.com/s/rswrysdxkuhfoh0/Movie%201%20Human.avi?dl=0> and Movie 2 at

<https://www.dropbox.com/s/kl1ctnxtraokbw/Movie%202%20Chick%20embryo.avi?dl=0>

and a lack of calibration of the inverse relationship between τ_c and flow velocity quantified by the proportionality constant α [23]. Several predictions for α have been suggested in literature, but disagree in their absolute value and physical dependence [24-26, 50]. The results of our study confirm that scatterer size and volume fraction influence the relationship between $1/\tau_c$ and V [26]. To quantitatively understand this relation we employed a theoretical model based on optical and physical properties of the scatterers, where α is particularly influenced by the scattering phase function and multiple scattering effects. The assumption that the scattering properties of RBCs in the microcirculation are invariant implies that rescaling for the number of scattering events is required for quantitative *in vivo* flowmetry. This has previously been implemented empirically by rescaling τ_c by a weighting term that is proportional to the vessel diameter [28]. We estimated the average number of scattering events with Monte Carlo simulations and related its distribution to the Mie-Percus-Yevick scattering model of whole blood. This approach resulted in an excellent agreement between theory and experiment, validating α *in vivo* for microcirculatory blood flow velocities and confirming the quantitative measure of flow velocity by LSCI. Conveniently, vessel diameters and vessel density can be estimated from the images, allowing quantitative mapping of both blood flow and velocity and estimating tissue perfusion using laser speckle flowmetry.

In Figs. 4.2 and 4.3 we systematically varied the size and volume fraction of flowing polystyrene spheres and compared the experimental and theoretical results. In Fig. 4.2b α for 5, 7 and 10 μm diameter particles (2.5 vol%) is in good agreement with our predictions, but for smaller scatterers (red colour shades) α is overestimated by theory. For the small scatterers (0.6, 1 and 2 μm), which are below the resolution limit of the system, α seems to saturate to a value of 2 - 2.5 μm^{-1} in our system. A similar value for α was found in our previous report, using 2.5 vol% Intralipid® as flowing fat emulsion with sub-resolution effective scatterer size [19]. Supplementary Fig. S4.7 shows that saturation of α is expected for small scatterers, albeit at much higher values. Moreover, α does not show dependence on volume fraction for these small spheres (Fig 4.2), suggesting that α in this case is predominantly determined by system properties rather than sample properties [16, 24]. On the other hand, from Supplementary table S4.1, all experiments with small particles involve a high μ_s and thus a large number of dynamic scattering events so that an alternative explanation is that our theory overestimates decorrelation by multiple scattering when the number of events get large. A satisfactory theoretical explanation for either possibility has hitherto not been found.

In our *in vivo* SDF-LSCI geometry, RBCs are above the resolution limit and in whole blood (high μ_s) multiple scattering is present in most vessels (our data set: $d = [10 - 55 \mu\text{m}]$, $N = [1 - 5]$) and N was low (<5) saturation of α is unlikely. Simulating N *in vivo* and applying the theoretical model to the optical properties of blood allowed to rescale the obtained τ_c for multiple scattering resulting in a high linear correlation between $1/\tau'_c$ and flow velocity. In addition, the measured α' is in perfect agreement with the theoretical prediction. Introducing the offset-decorrelation correction to conventional LSCI analysis yields a quantitative decorrelation map (Fig. 4.5b) and subsequently applying the model-based scaling factor yields a quantitative blood velocity map (Fig. 4.5c). Though *in vivo* α' could only be validated against low flow velocities ($< 2 \text{ mm/s}$) measured by conventional SDF flowmetry,

the *in vitro* experiments verified a' up to 15 mm/s indicating that LSCI is capable of measuring high microcirculatory flow velocities as well. Extending the multi-exposure regime to lower exposure times will increase the maximum flow velocity limit further.

The variance in the estimation of N with Monte Carlo simulations is due to uncertainties in the included optical properties and fidelity of the simulated measurement geometry. Our phantom experiment offers an alternative way to validate N as described in Supplementary Section 4.9 and Supplementary Fig. S4.8. The latter also illustrates the importance of including the parameter ρ to obtain τ_c from the speckle contrast K . Naturally, different geometries result in different ρ (e.g. due to different static/dynamic medium properties, tube diameter, etc.) thus ρ needs appropriate estimation/calibration. *In vivo*, ρ is influenced by geometry, vessel diameter, vessel depth and Hct values and can be estimated using long exposure times. When neglecting to appropriately estimate ρ the resulting value for τ_c can deviate majorly [28, 44]. Estimation of N *in vivo* using Monte Carlo simulations depends on the geometrical and optical properties such as vessel depth, diameter and $\mu_{s,blood}$. Varying the vessel depth between 0.1 and 0.4 mm and the Hct between 30% and 45% resulted in comparable values for N (Supplementary Fig. S4.3), indicating that the estimation of N is robust. In addition, calculating a' using these varying N values influenced a' by less than ± 0.02 for microcirculatory vessel diameters. Alternatively, low-coherence interferometric set-ups allow path-length resolved speckle signals to be acquired [50-52], providing better estimation of N albeit without the simplicity of the LSCI approach.

To make our results more widely applicable we performed Monte Carlo simulations for a conventional speckle imaging set-up where wide field laser light illuminates tissue at an angle and the backscattered light is captured by a camera directly above the tissue [10, 13, 14, 27, 28, 53]. In this geometry very similar N values for dynamic detected photons were found for both *in vitro* and *in vivo* optical properties (Supplementary Fig. S4.3), which generalizes our multiple scattering correction. As a practical guideline we therefore plotted the *in vivo* scaling factor $A(N)$ for two Hct values in Fig. 4.6, solid lines. For comparison to conventional LSCI approaches we also plotted $A(N)$ for Gaussian and Lorentzian shape of $g_1(\tau)$ (dashed lines), calculated using a normal distribution for $p(n)$. Rescaling for multiple scattering is thus highly model dependent, where the Lorentzian ($A(N) \sim N$) and the Gaussian ($A(N) \sim \sqrt{N}$) model result in an underestimation or overestimation of V , respectively. Thus, the practical realization of quantitative laser speckle flowmetry necessitates the estimation of N from the geometry of blood vessels. Then, τ_c' is calculated according to $1/\tau_c' = (1/\tau_c)/A(N)$ and the flow velocity estimated from $1/\tau_c' \approx [0.38 \pm 0.04]V$. We emphasize that τ_c *in vivo* is subject to additive decorrelation sources along the photon path through tissue [19], which should be estimated and corrected accordingly.

We use the analytical model of Supplementary Eq. (4.10) to fit experimental $K(T)$ vs. T curves, based on the *ansatz* that this model accurately retrieves the actual decorrelation time τ_d , even though our derived $g_1(\tau)$ is not necessarily purely Gaussian. We verified the validity of this approach by calculation (Supplementary Section S4.10). It is shown that the current model and the Gaussian model approximate each other sufficiently, especially for $N > 1$, by examining the final $K(T)$ curve. We therefore conclude that assuming a Gaussian ACF, thereby making the model analytical and practical, results in an acceptably small er-

ror in τ_c . This result does not imply that scaling factors $A(N)$ should be based on Gaussian approximations to $g_1(\tau)$ as evidenced by Fig. 4.6. We therefore scale our *in vivo* measured τ_c to the value τ'_c (for single scattering) using the model-based factor $A(N)$.

The approach to calculate g_1 for multiple scattering has been recognized in literature [50, 52, 54], explicitly in the LDF [26] and DWS [33] field. The differences in the treatment of multiple scattering and modelling g_1 between LDF, DWS and our approach are discussed in Supplementary Section S4.11. Key challenges are to find a valid model for g_1 and a valid expression for $p(n)$ in the specific geometry. Here we have shown that our experimental a' (and estimation of $p(n)$) matches brilliantly with theory ($a' = 0.38$) and falls in between predictions from the LDF framework ($a'_{LDF} = 0.36$) and DWS framework ($a'_{DWS} = 0.54$).

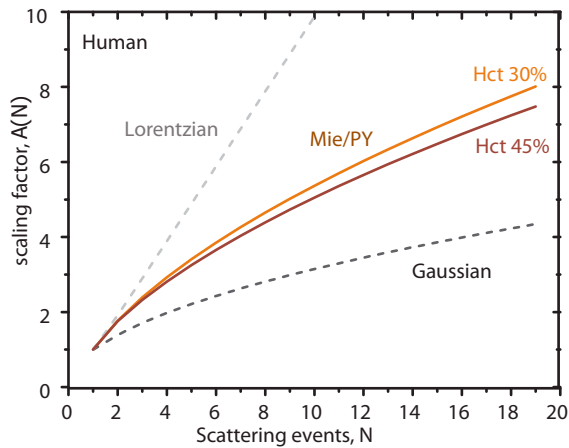


Figure 4.6 | Multiple scattering scaling factor. Scaling factor $A(N)$ for a is calculated using our model based on Mie/PY scattering in human blood for Hct = 30% (orange line) and Hct = 45% (red line). Dashed lines represent $A(N)$ for Lorentzian (grey) and Gaussian (black) models for g_1 . All scaling factors are calculated using a normal distribution for $p(n)$.

The experimental and theoretical findings in this study improve the quantitative flowmetry capabilities of LSCI and show that the clinically relevant parameters blood flow, velocity and tissue perfusion, can be quantitatively represented in SDF-LSCI microcirculation images, escaping the doctrine of qualitative and relative flow measures. This enables SDF-LSCI to quantitatively study microcirculation within and between organs and organisms and during the course of disease and therapy. In essence, for quantitative *in vivo* speckle flowmetry reliable calculation of τ_c , correction for ‘offset’ decorrelation [19], and estimation of vessel diameter to correct for multiple scattering are key ingredients. We recommend to consider the influence of system resolution on a , for example when choosing flowing scattering solutions in phantom experiments. The highly vascularized chorioallantoic membrane of the chick embryo can be a practical calibration model as an intermediate between *in vitro* and *in vivo* validation.

4.6 ACKNOWLEDGMENTS

The authors kindly thank Microscan B.V. (Amsterdam) for providing a modified Microscan and financial support. A.N. gratefully acknowledges the financial support from the Gerbrand de Jong Fonds (the Netherlands). Part of this work was sponsored by Technology Foundation STW under the *iMIT* programme

4.7 REFERENCES

1. B. Fagrell and M. Intaglietta, "Microcirculation: its significance in clinical and molecular medicine," *J. Intern. Med.* **241**, 349-362 (1997).
2. C. Ince, "The microcirculation is the motor of sepsis," *Critical Care* **9**, S13 (2005).
3. A. Villringer and U. Dirnagl, "Coupling of brain activity and cerebral blood flow: basis of functional neuroimaging," *Cerebrovasc. Brain Metab. Rev.* **7**, 240-276 (1994).
4. K. R. Mathura, G. J. Bouma, and C. Ince, "Abnormal microcirculation in brain tumours during surgery," *The Lancet* **358**, 1698-1699 (2001).
5. J. A. Lindeboom, K. R. Mathura, and C. Ince, "Orthogonal polarization spectral (OPS) imaging and topographical characteristics of oral squamous cell carcinoma," *Oral oncology* **42**, 581-585 (2006).
6. K. E. Emblem, K. Mouridsen, A. Bjornerud, C. T. Farrar, D. Jennings, R. J. Borra, P. Y. Wen, P. Ivy, T. T. Batchelor, and B. R. Rosen, "Vessel architectural imaging identifies cancer patient responders to anti-angiogenic therapy," *Nature medicine* **19**, 1178-1183 (2013).
7. J. Folkman, "Angiogenesis in cancer, vascular, rheumatoid and other disease," *Nature medicine* **1**, 27-30 (1995).
8. P. Carmeliet and R. K. Jain, "Angiogenesis in cancer and other diseases," *Nature* **407**, 249-257 (2000).
9. A. Fercher and J. Briers, "Flow visualization by means of single-exposure speckle photography," *Opt. Commun.* **37**, 326-330 (1981).
10. A. K. Dunn, H. Bolay, M. A. Moskowitz, and D. A. Boas, "Dynamic imaging of cerebral blood flow using laser speckle," *Journal of Cerebral Blood Flow & Metabolism* **21**, 195-201 (2001).
11. A. B. Parthasarathy, E. L. Weber, L. M. Richards, D. J. Fox, and A. K. Dunn, "Laser speckle contrast imaging of cerebral blood flow in humans during neurosurgery: a pilot clinical study," *Journal of biomedical optics* **15**(2010).
12. H. Knotzer and W. R. Hasibeder, "Microcirculatory function monitoring at the bedside—a view from the intensive care," *Physiol. Meas.* **28**, R65 (2007).
13. P. Li, S. Ni, L. Zhang, S. Zeng, and Q. Luo, "Imaging cerebral blood flow through the intact rat skull with temporal laser speckle imaging," *Opt. Lett.* **31**, 1824-1826 (2006).
14. C. Ayata, A. K. Dunn, Y. Gursoy-Özdemir, Z. Huang, D. A. Boas, and M. A. Moskowitz, "Laser speckle flowmetry for the study of cerebrovascular physiology in normal and ischemic mouse cortex," *Journal of Cerebral Blood Flow & Metabolism* **24**, 744-755 (2004).
15. D. Briers, D. D. Duncan, E. Hirst, S. J. Kirkpatrick, M. Larsson, W. Steenbergen, T. Stromberg, and O. B. Thompson, "Laser speckle contrast imaging: theoretical and practical limitations," *Journal of biomedical optics* **18**, 066018-066018 (2013).
16. D. D. Duncan and S. J. Kirkpatrick, "Can laser speckle flowmetry be made a quantitative tool?," *JOSA A* **25**, 2088-2094 (2008).
17. J. D. Briers and S. Webster, "Laser speckle contrast analysis (LASCA): a non-scanning, full-field technique for monitoring capillary blood flow," *Journal of biomedical optics* **1**, 174-179 (1996).
18. J. W. Goodman, *Speckle phenomena in optics: theory and applications* (Roberts and Company Publishers, Greenwood Village, CO, 2007).
19. A. Nadort, R. G. Woolthuis, T. G. van Leeuwen, and D. J. Faber, "Quantitative laser speckle flowmetry of the *in vivo* microcirculation using sidestream dark field microscopy," *Biomedical optics express* **4**, 2347-2361 (2013).
20. O. B. Thompson and M. K. Andrews, "Tissue perfusion measurements: multiple-exposure laser speckle analysis generates laser Doppler-like spectra," *Journal of biomedical optics* **15**, 027015-027015-027017 (2010).
21. P. Goedhart, M. Khalilzadea, R. Bezemer, J. Merza, and C. Ince, "Sidestream Dark Field (SDF) imaging: a novel stroboscopic LED ring-based imaging modality for clinical assessment of the microcirculation," *Opt. Express* **15**, 15101-15114 (2007).
22. W. Groner, J. W. Winkelman, A. G. Harris,

- C. Ince, G. J. Bouma, K. Messmer, and R. G. Nadeau, "Orthogonal polarization spectral imaging: a new method for study of the microcirculation," *Nature medicine* **5**, 1209-1213 (1999).
23. M. Draijer, E. Hondebrink, T. Van Leeuwen, and W. Steenbergen, "Review of laser speckle contrast techniques for visualizing tissue perfusion," *Lasers in medical science* **24**, 639-651 (2009).
 24. T. Yoshimura, "Statistical properties of dynamic speckles," *JOSA A* **3**, 1032-1054 (1986).
 25. J. D. Briers, G. Richards, and X. W. He, "Capillary blood flow monitoring using laser speckle contrast analysis (LASCA)," *Journal of biomedical optics* **4**, 164-175 (1999).
 26. R. Bonner and R. Nossal, "Model for laser Doppler measurements of blood flow in tissue," *Applied optics* **20**, 2097-2107 (1981).
 27. T. Durduran, M. G. Burnett, G. Yu, C. Zhou, D. Furuya, A. G. Yodh, J. A. Detre, and J. H. Greenberg, "Spatiotemporal quantification of cerebral blood flow during functional activation in rat somatosensory cortex using laser-speckle flowmetry," *Journal of Cerebral Blood Flow & Metabolism* **24**, 518-525 (2004).
 28. S. M. S. Kazmi, A. B. Parthasarthy, N. E. Song, T. A. Jones, and A. K. Dunn, "Chronic imaging of cortical blood flow using Multi-Exposure Speckle Imaging," *Journal of Cerebral Blood Flow & Metabolism* **33**, 798-808 (2013).
 29. G. A. Armitage, K. G. Todd, A. Shuaib, and I. R. Winship, "Laser speckle contrast imaging of collateral blood flow during acute ischemic stroke," *Journal of Cerebral Blood Flow & Metabolism* **30**, 1432-1436 (2010).
 30. M. Roustit, C. Millet, S. Blaise, B. Dufournet, and J. Cracowski, "Excellent reproducibility of laser speckle contrast imaging to assess skin microvascular reactivity," *Microvascular Research* **80**, 505-511 (2010).
 31. M. Stern, "In vivo evaluation of microcirculation by coherent light scattering," *Nature* **254**, 56-58 (1975).
 32. D. Pine, D. Weitz, P. Chaikin, and E. Herbolzheimer, "Diffusing wave spectroscopy," *Physical Review Letters* **60**, 1134 (1988).
 33. D. Weitz, J. Zhu, D. Durian, H. Gang, and D. Pine, "Diffusing-wave spectroscopy: The technique and some applications," *Physica Scripta* **1993**, 610 (1993).
 34. N. Bosschaart, G. J. Edelman, M. C. Aalders, T. G. van Leeuwen, and D. J. Faber, "A literature review and novel theoretical approach on the optical properties of whole blood," *Lasers in medical science* **29**, 453-479 (2014).
 35. J. K. Percus and G. J. Yevick, "Analysis of classical statistical mechanics by means of collective coordinates," *Physical Review* **110**, 1 (1958).
 36. M. Wertheim, "Exact solution of the Percus-Yevick integral equation for hard spheres," *Physical Review Letters* **10**, 321-323 (1963).
 37. V. D. Nguyen, D. Faber, E. van der Pol, T. van Leeuwen, and J. Kalkman, "Dependent and multiple scattering in transmission and back-scattering optical coherence tomography," *Opt. Express* **21**, 29145-29156 (2013).
 38. J.-P. Hansen and I. R. McDonald, *Theory of Simple Liquids* (Elsevier, Amsterdam, 1990).
 39. L. Tsang, J. A. Kong, and K.-H. Ding, *Scattering of Electromagnetic Waves, Theories and Applications* (John Wiley & Sons, New York, 2004), Vol. 27.
 40. R. Bandyopadhyay, A. Gittings, S. Suh, P. Dixon, and D. Durian, "Speckle-visibility spectroscopy: A tool to study time-varying dynamics," *Review of scientific instruments* **76**, 093110-093110-093111 (2005).
 41. P. Zakharov, A. Völker, A. Buck, B. Weber, and F. Scheffold, "Quantitative modeling of laser speckle imaging," *Opt. Lett.* **31**, 3465-3467 (2006).
 42. D. A. Boas and A. K. Dunn, "Laser speckle contrast imaging in biomedical optics," *Journal of biomedical optics* **15**(2010).
 43. O. Thompson, M. Andrews, and E. Hirst, "Correction for spatial averaging in laser speckle contrast analysis," *Biomedical optics express* **2**, 1021-1029 (2011).
 44. A. B. Parthasarathy, W. J. Tom, A. Gopal, X. Zhang, and A. K. Dunn, "Robust flow measurement with multi-exposure speckle imaging," *Opt. Express* **16**, 1975-1989 (2008).
 45. S. J. Kirkpatrick, D. D. Duncan, and E. M. Wells-Gray, "Detrimental effects of speckle-pixel size matching in laser speckle contrast imaging," *Opt. Lett.* **33**, 2886-2888 (2008).
 46. J. G. G. Dobbe, G. J. Streekstra, B. Atasever, R. Van Zijderveld, and C. Ince, "Measurement of functional microcirculatory geometry and velocity distributions using automated image analysis," *Medical and Biological Engineering and Computing* **46**, 659-670 (2008).
 47. D. M. de Bruin, R. H. Bremmer, V. M. Kodach, R. de Kinkelder, J. van Marle, T. G. van Leeuwen, and D. J. Faber, "Optical phantoms of varying geometry based on thin building blocks with controlled optical properties," *Journal of biomedical optics* **15**, 025001 (2010).
 48. D. S. Dohle, S. D. Pasa, S. Gustmann, M. Laub,

- J. H. Wissler, H. P. Jennissen, and N. Dünker, "Chick ex ovo culture and ex ovo CAM assay: how it really works," *Journal of visualized experiments: JoVE* (2009).
49. A. R. Pries, T. W. Secomb, P. Gaehtgens, and J. Gross, "Blood flow in microvascular networks. Experiments and simulation," *Circul. Res.* **67**, 826-834 (1990).
 50. A. Wax, C. Yang, R. R. Dasari, and M. S. Feld, "Path-length-resolved dynamic light scattering: modeling the transition from single to diffusive scattering," *Applied optics* **40**, 4222-4227 (2001).
 51. J. Kalkman, R. Sprik, and T. van Leeuwen, "Path-length-resolved diffusive particle dynamics in spectral-domain optical coherence tomography," *Physical Review Letters* **105**, 198302 (2010).
 52. K. K. Bizheva, A. M. Siegel, and D. A. Boas, "Path-length-resolved dynamic light scattering in highly scattering random media: The transition to diffusing wave spectroscopy," *Physical Review E* **58**, 7664 (1998).
 53. B. Choi, N. M. Kang, and J. S. Nelson, "Laser speckle imaging for monitoring blood flow dynamics in the *in vivo* rodent dorsal skin fold model," *Microvascular Research* **68**, 143-146 (2004).
 54. T. B. Rice, E. Kwan, C. K. Hayakawa, A. J. Durkin, B. Choi, and B. J. Tromberg, "Quantitative, depth-resolved determination of particle motion using multi-exposure, spatial frequency domain laser speckle imaging," *Biomedical optics express* **4**, 2880-2892 (2013).

SUPPLEMENTARY INFORMATION

S4.1 THEORY

S4.1a Optical and physical properties of the dynamic medium

We briefly review the optical properties relevant to our application. We model our phantom and tissue as a discrete random medium of hard spheres (i.e. occupying non-overlapping volumes). The differential scattering cross section $\sigma_{\text{sca}}(\mathbf{q})$ describing the angular distribution of scattered light by a single sphere, is calculated using Mie (M) theory [1]. Here $\mathbf{q} = \mathbf{k}_{\text{sca}} - \mathbf{k}_{\text{in}}$ is the scattering vector with magnitude $|\mathbf{q}| = 2k\sin(\theta/2)$; k is the wavenumber $2\pi/\lambda$ and θ is the scattering angle. To account for inter-particle correlation effects (“dependent scattering”), we calculate the structure factor $S(\mathbf{q})$ using the Percus-Yevick (PY) equation [2] for hard spheres [3]. The scattering coefficient μ_s , cross section σ_{sca} and scattering phase function $p(\mathbf{q})$ are then found, respectively, as:

$$\mu_{s,MPY} = \eta\sigma_{\text{sca},MPY} = \eta 2\pi \int_0^{2k} \sigma_{\text{sca},MIE}(\mathbf{q}) S_{PY}(\mathbf{q}, f_v) \mathbf{q} d\mathbf{q} \quad (4.1a)$$

$$p_{MPY}(\mathbf{q}) = \frac{\sigma_{\text{sca},MIE}(\mathbf{q}) S_{PY}(\mathbf{q}, f_v)}{\sigma_{\text{sca},MPY}} \quad (4.1a)$$

Here $\eta = f_v/V_p$ is the particle number density in the medium; with f_v the volume fractions of particles with volume V_p . The structure factor is given by the Fourier transform of the pair correlation function PCF(r) which is interpreted as the distribution of distances r between particle pairs. For dilute solutions of hard spheres of diameter D , PCF(r) = 0 when $r < D$ and unity otherwise. For higher volume fractions PCF(r) shows damped oscillatory behaviour, with increased probability of finding pair separations at multiples of D and decreased probability in between. In the limit $r \rightarrow \infty$; PCF(r) goes to unity. The structure factor $S(\mathbf{q})$ is approximately constant at unity for low volume fractions. Non-unity $S(\mathbf{q})$ at higher values of f_v cause an angular redistribution of scattered light (Eq. (4.1b)) as well as non-linear scaling of the scattering coefficient.

S4.1b Dependence of τ_c on the optical properties of the dynamic medium

Consider an ensemble of scatterers (indexed j) each moving with velocity \mathbf{V}_j in a vessel within an otherwise static, scattering medium. The velocity distribution is given by $p(\mathbf{V})$. The normalized electric field autocorrelation (ACF) function $g_1(\tau) = \langle E^*(t+\tau)E(t) \rangle_r / \langle E(t)E^*(t) \rangle_r$, for a single scattering event from moving particles is [4]:

$$g_{1,\text{single}}(\mathbf{q}, \tau) = \left\langle \sum_i \exp(-i\mathbf{q} \cdot \mathbf{V}_i \tau) \right\rangle \quad (4.2)$$

When light undergoes many scattering events before reaching the vessel, the propagation direction becomes isotropic. Consequently, the direction of the scattering vector \mathbf{q} with respect to the velocity vector \mathbf{V} also becomes isotropic, and the velocity distribution de-

pends only on the magnitude $|\mathbf{V}|=V$. We assume a Gaussian-shaped speed distribution $p(V) = \sqrt{(2/\pi)} (3/V_0)^{3/2} \exp(-3V^2/2V_0^2)$; where V_0 is the average flow velocity. Averaging over $p(V)$ yields [4-6]:

$$g_{1,\text{single}}(\mathbf{q}, \tau) = \exp\left(-q^2 V_0^2 \tau^2 / 6\right) \quad (4.3)$$

In the following, we drop the subscript '0' on velocity. The average over \mathbf{q} is calculated as:

$$g_{1,\text{single}}(\tau) = \int_0^{2k} p_{MPY}(\mathbf{q}) \exp\left(-q^2 V^2 \tau^2 / 6\right) q d\mathbf{q} \quad (4.4)$$

The angular weighting by the phase function of Supplementary Eq. (4.1b), introduces dependence on the optical and physical properties in g_1 (and thus in τ_c).

S4.1c Multiple scattering

Eq. (4.4) describes the electric field decorrelation due to single scattering events. If subsequent scattering events are assumed to be statistically independent, the ACF becomes $[g_1(\tau)]^n$ where n is the number of scattering events from moving scatterers. The total correlation function follows after weighting with the appropriate distribution of n :

$$g_1(\tau) = \sum_{n=1}^{\infty} p(n) [g_{1,\text{single}}(\tau)]^n \quad (4.5)$$

Because the scattering events take place at the particles, the distribution $p(n)$ in the measurement volume follows the microscopic distribution of the number of particles $p(\eta_{\text{micr}})$ in the dynamic medium. If the particles positions are independent of each other, $p(\eta_{\text{micr}})$ and $p(n)$ are given by the Poisson distribution [7], with equal mean and variance of $\langle \eta_{\text{micr}} \rangle = \sigma^2 \eta_{\text{micr}} = \eta$ (the global average density); and of $\langle n \rangle = \sigma_n^2 = N$, respectively. When correlations between the particle positions are present, e.g. when $\text{PCF}(r) \neq 1$, the Poissonian distribution model is no longer valid. Although the exact distribution is unknown, the relation between mean (N) and variance (σ_n^2) is determined by the PCF as [8, 9]:

$$\frac{\sigma_n^2}{N} = 1 + \eta \int [PCF_{PY}(r) - 1] dr = \frac{(1-f_v)^4}{(1+2f_v)^2} \quad (4.6)$$

Where the right-hand side is valid for the PY equation of $\text{PCF}(r)$ for hard spheres. In our present analysis, we assume $p(n)$ follows a normal distribution where the relation between mean and variance is given by Eq. (4.6). Parameter N is estimated from Monte Carlo simulation of our experimental geometry (Supplementary Section 4.3) The ACF $g_1(\tau)$ is an exponentially decaying function of time, parameterized by the characteristic timescale τ_c (decorrelation time) which is evaluated from [4, 7]:

$$\tau_c = \int_0^{\infty} g_1(\tau) d\tau \quad (4.7)$$

Following the above outlined exercise, g_1 can be plotted according to the set of optical and physical properties (including N) and the proportionality constant α can be derived as $1/\tau_c$ at $V = 1$. The ACF calculated using the above formulae is of Gaussian form (because all involved functionals, i.e. phase function, velocity distribution and distribution of the number of scattering events, are of (near) Gaussian shape). In the following, we therefore assume that $g_1(\tau) = \exp(-0.25\pi(\tau/\tau_c)^2)$ for mathematical convenience of the procedure to extract τ_c from spatial speckle contrast measurements (Supplementary Section 4.1d). The validity of this approximation is discussed in Supplementary Section S4.10.

S4.1d Spatial assessment of temporal speckle dynamics

Laser Speckle Contrast Imaging (LSCI) assesses sample dynamics from spatial measurement of speckle contrast, defined as the ratio of the standard deviation (σ_i) to the mean ($\langle I \rangle$) of the intensity:

$$K = \frac{\sigma_i}{\langle I \rangle} \quad (4.8)$$

This quantity is related to sample dynamics through temporal integration of the ACF $g_1(\tau)$ as obtained from Supplementary Eq. (4.5) [7]:

$$K(T) = \beta_M^{1/2} \left[\frac{2}{T} \int_0^T \left(1 - \frac{\tau}{T} \right) |g_1(\tau)|^2 d\tau \right]^{1/2} \quad (4.9)$$

Here, T is the exposure time of the camera and β_M is a measurement-geometry specific constant that can be calibrated [10]. In the general case of flow in a single vessel or channel, $g_1(\tau)$ is assumed to have a Gaussian form $g_1(\tau) = \exp(-0.25\pi(\tau/\tau_c)^2)$ as described in Supplementary Section 4.1c. For Brownian motion, $g_1(\tau)$ takes a Lorentzian form: $g_1(\tau) = \exp(-\tau/\tau_c)$. A sampled biological tissue volume likely consist of both static and dynamic scatterers. The influence of the static component on $g_1(\tau)$ can be taken into account [11-13] by introducing a dependence on I_s , with I_f the detected intensity of the fluctuating scattered light and I_s the detected intensity of the light scattered by static components. The speckle contrast Supplementary Eq. (4.9) can be solved analytically for the Gaussian form of $g_1(\tau)$ to give [11, 12]:

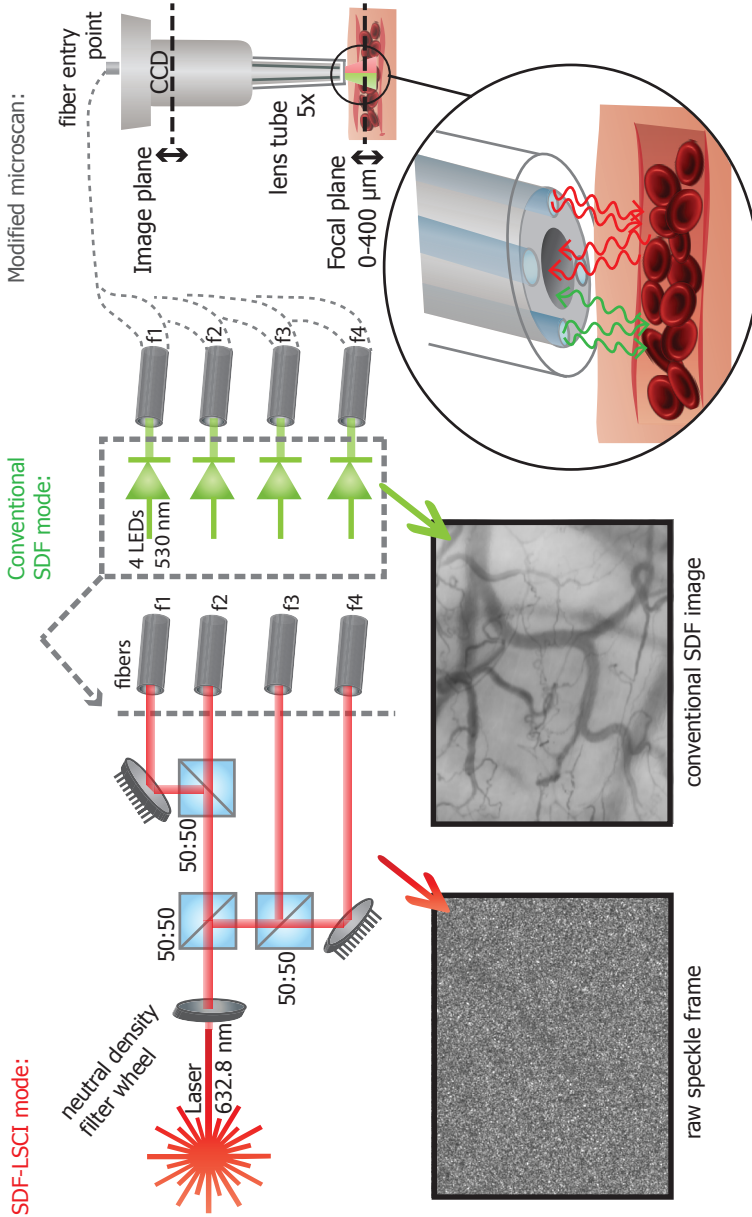
$$K(x) = \beta^{1/2} \left[\rho^2 \frac{\exp(-2(x)^2) - 1 + \sqrt{2\pi} x \operatorname{erf}(\sqrt{2}x)}{2(x)^2} + 2\rho(1-\rho) \frac{\exp(-(x)^2) - 1 + \sqrt{\pi} x \operatorname{erf}(x)}{(x)^2} + (1-\rho)^2 \right]^{1/2} + C_{\text{noise}} \quad (4.10)$$

where $x = \sqrt{\pi T/2\tau_{c,\text{total}}}$ and C_{noise} an added noise term for measurement noise. For our determination of $\tau_{c,\text{total}}$ we fit the model of Supplementary Eq. (4.10) to measurements of K obtained with different exposure times as detailed in Methods. The definition of x differs a factor $\sqrt{\pi}/2$ from other publications and Chapter 3 [10, 14, 15] in which $g_1(\tau) = \exp(-(\tau/\tau_c)^2)$ is used – a form that is incompatible with our Supplementary Eq. (4.7). In biological tissue $\tau_{c,\text{total}}$ represents the total decorrelation due to contributions from ‘offset’ (e.g. muscle movements) and the desired flow dynamics.

S4.2 SIDESTREAM DARK FIELD AND LASER SPECKLE CONTRAST IMAGING (SDF-LSCI)

SET UP

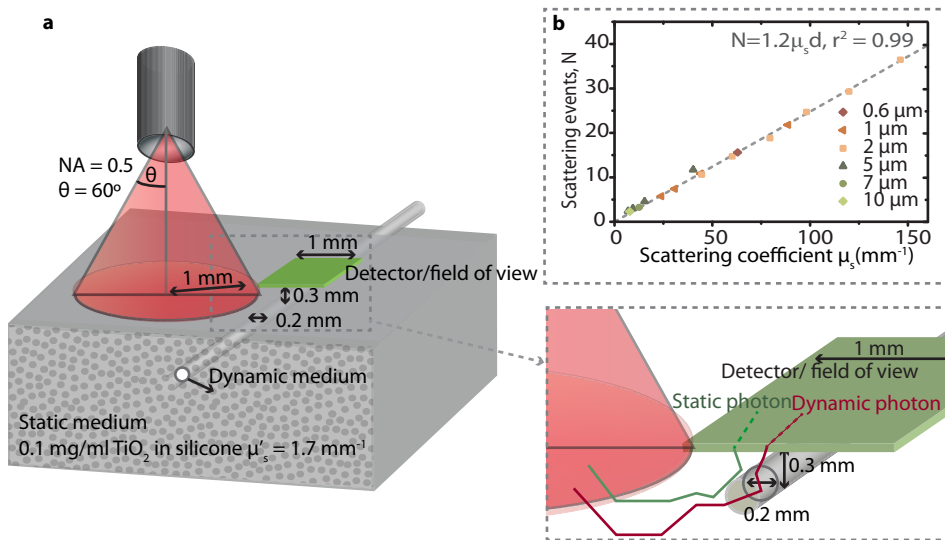
To enable absolute blood flow measurements and estimation of τ_c of the same *in vivo* vessels we modified a clinical microcirculation imager (Microscan, Microvision Medical, The Netherlands) to allow illumination by different light sources [10]. The conventional system provides illumination by six green LEDs at the tip of the lens tube, which were replaced by four optical fibres (POF ESKA, fibre core 980 μm , NA 0.5). The fibres are directed through the imager alongside the lens tube, which is covered with a sterile cap and can be brought into contact with the tissue of interest. In SDF-LSCI mode, as is shown in Supplementary Fig. S4.1, laser light (632.8 nm, He/Ne, Spectra Physics, US) is split into four beams by three 50:50 beam splitters and coupled into the four multimode fibres. Raw speckle frames with different exposure times are captured by a monochrome camera at 30 frames per second (IEEE 1394, Guppy F-080B, Allied Vision Technologies, Germany), controlled by self-written software (LabVIEW, National Instruments, US). For exposure times above 33 ms obviously the frame rate is less. Overexposure is prevented by a neutral density filter wheel in front of the laser. In conventional SDF mode the fibres are illuminated by four LEDs (530 \pm 20 nm). Conventional SDF images show good contrast between tissue and highly absorbing red blood cells (RBCs). Conventional and SDF-LSCI mode were consecutively employed to image the same microcirculation area. The focal plane can be translated between tissue surface and 0.4 mm depth and the optical magnification is 5x.



Supplementary Figure S4.1 | Dual-mode non-invasive microcirculation imaging set-up. SDF-LSCI mode: speckle contrast due to reflection of coherent laser light by flowing RBCs and 'static' tissue. Conventional SDF mode: contrast due to absorption of green light by flowing RBCs. See text left for more details.

S4.3 MONTE CARLO SIMULATIONS TO ESTIMATE N

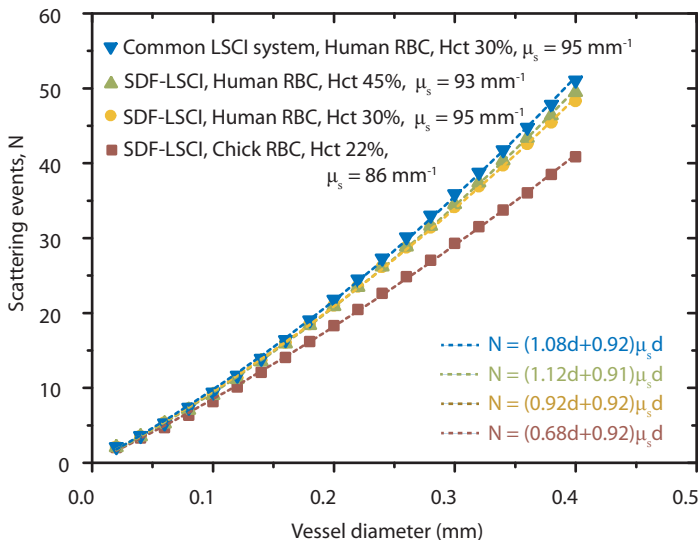
To get a reliable estimate for the number of dynamic scattering events, N , we built the geometry in Monte Carlo simulation freeware [16, 17], and included the scattering coefficients of the static phantom and dynamic polystyrene spheres for all sizes and volume fractions (see Supplementary table S4.2), as shown in Supplementary Fig. S4.2. Photon transport was simulated for one fibre, and the results were rotated 90, 180 and 270 degrees to mimic 1 fibre in each corner. In this set-up the optical absorption is low and can be ignored. The number of Doppler events are stored per detected photon. We simulated 5000 dynamic photons (thus photons with at least 1 scattering event in the flow tube) detected at the centre of the tube/vessel region in the field of view and calculated the average number or Doppler scattering events, N , per dynamic photon. The relationship between μ_s and N could be linearly fitted by $N = 1.2\mu_s d$, ($r^2 = 0.99$) for 15 different simulations with μ_s ranging from 20 - 150 mm^{-1} and d the tube diameter of 0.2 mm (see Supplementary Fig. S4.2b). The factor $F = 1.2$ [95% upper CI - lower CI: 1.21 - 1.26, CI confidence interval] is likely due to an increased effective optical path length as a result of scattering, photons crossing the tube with a longitudinal component, and photons crossing the tube more than once. For low μ_s ($< 20 \text{ mm}^{-1}$) the factor was slightly higher (< 1.9), due to a low number of scattering events in the tube ($N < 5$) and subsequent overestimation of the photon path through the tube. We therefore fixed the factor at 1.2 for all μ_s and this specific d of 0.2 mm.



Supplementary Figure S4.2 | Monte Carlo geometry and simulation in vitro. (a) To mimic the SDF geometry a diverging beam is located at ~ 1 mm distance from the detector field representing a high NA fibre and photons are launched into the static medium (TiO_2 in silicone). The flow tube with optical properties for polystyrene spheres is placed in the medium (diameter 0.2 ± 0.03 mm; depth $0.3 \text{ mm} \pm 0.03$ mm). The simulation results are rotated to represent a fibre in each corner. For each photon detected at the centre of the tube (in the detector plane) the number of Doppler scattering events N is counted, and the average N per detected photon is plotted versus scattering coefficient in (b), as well as a linear fit to the data (dashed line).

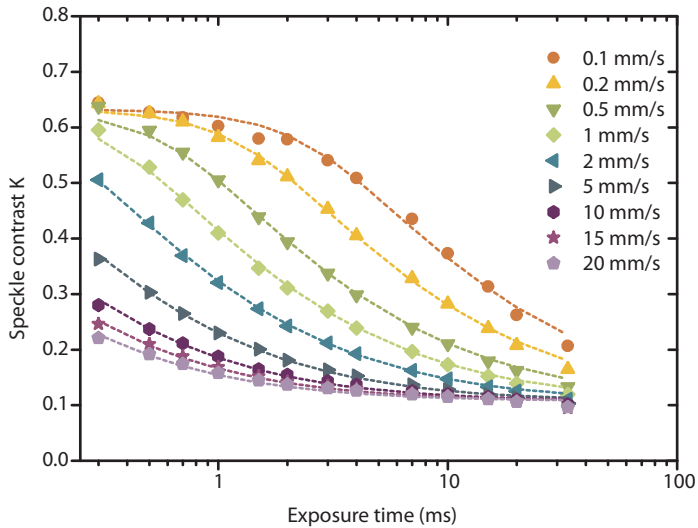
The number of scattering events in the *in vivo* vessels was also estimated using Monte Carlo simulations with the same geometry as shown in Supplementary Fig. S4.2 adapted to the scattering properties of blood. The optical properties of human blood are reviewed by Bosschaert et al.[18]. We calculated the optical properties accordingly, taking into account a reduced microcirculatory hematocrit (Hct) as a result of the Fahraeus effect [19] (average microcirculatory Hct = 30%, see Supplementary table S4.1), for a range of vessel diameters [0.02 - 0.4 mm]. The resulting N can be described by $N = (0.92d+0.92)\mu_s d$, with d in mm and $\mu_s = 95 \text{ mm}^{-1}$. For chick embryo whole blood no experimentally validated optical properties were found, therefore, we estimated the optical properties using the known red blood cell volume [20] and hematocrit [21] calculated using Mie scattering and Pervus-Yevick theories [1, 3], see Supplementary table S4.1. Inserting these value into the Monte Carlo geometry resulted in $N = (0.68d+0.92)\mu_s d$, with $\mu_s = 86 \text{ mm}^{-1}$. To find N the *in vivo* vessel diameters can be estimated from conventional SDF images.

To generalize our results, we simulated two other scenarios: 1. N for vessels with full hematocrit (Hct = 45%) and 2. N for a common LSCI system geometry. In most LSCI systems, the laser light illuminates the tissue at a 45° angle and the detector is placed perpendicularly above the tissue. For all situations similar values for N were found, as is plotted in Supplementary Fig. S4.3 below.



Supplementary Figure S4.3 | *In vivo* scattering events from Monte Carlo simulations. The average N per detected dynamic photon for a range of vessel diameters was obtained from Monte Carlo simulations using *in vivo* optical properties for human (Hct 30% (yellow circles) and Hct 45% (green triangles)) and chick embryo (Hct 22% (red squares)) blood, see Supplementary table 1. In addition, N was simulated for a common LSCI system where the laser beam is directly illuminating the tissue at a 45° angle and the camera is placed perpendicularly above the tissue (blue upside down triangles). Polynomial curve fits are plotted as dashed lines and the fit coefficients are displayed (all $r^2 > 0.99$).

S4.4 MULTI-EXPOSURE CURVES AND FITS



Supplementary Figure S4.4 | Multi-exposure curves and fits. Multi-exposure speckle contrast values (data points) and corresponding fit of Supplementary Eq. (4.10) (dashed lines) for 9 different flow velocities for $2\ \mu\text{m}$ polystyrene spheres (2.5 vol%). Speckle contrast K is calculated according to Supplementary Eq. (4.8), for a local region of 10×10 spatial pixels. No error bars are shown for clarity. At least 200 K -values in the centre of the tube were selected and the standard deviation in was K less than 5%.

S4.5 OPTICAL PROPERTIES OF SCATTERERS

Supplementary table S4.1 and S4.2 list the optical properties of scatterers used in the *in vivo* and *in vitro* experiments. To estimate the error in theoretical a we varied the size of the polystyrene spheres by $\pm 10\%$ and the refractive index by $\pm 5\%$, as this variation was reported for the purchased polystyrene spheres (Kisker-Biotech, Germany) [22]. For the red blood cells (RBCs) we varied the size by $\pm 5\%$ and refractive index by $\pm 1\%$.

 Table S4.1. Optical properties of scatterers at 632.8 nm^a

	Refractive index particle	Refractive index medium	Scatterer diameter	Vol %	Scattering coefficient	g^b
Human blood, microcirculation	$n_{RBC} = 1.3937^c$	$n_{plasma} = 1.345^c$	$5.6 \mu\text{m}^d$	30%	$\mu_{s,blood} = 95 \text{ mm}^{-1}$	0.991
Human blood	$n_{RBC} = 1.3937^c$	$n_{plasma} = 1.345^c$	$5.6 \mu\text{m}^d$	45%	$\mu_{s,blood} = 93 \text{ mm}^{-1}$	0.986
Chick blood, microcirculation	$n_{RBC} = 1.3937^c$	$n_{plasma} = 1.345^c$	$7.1 \mu\text{m}^d$	22% ^e	$\mu_{s,blood,chick} = 42 \text{ mm}^{-1}$	0.993
TiO ₂ in silicone	$n_{TiO_2} = 2.49^f$	$n_{silicone} = 1.4225^f$	$\sim 0.2 \mu\text{m}^f$	0.0265% (1 mg/ml)	$\mu_{s,phantom} = 4.1 \text{ mm}^{-1}$	0.58
Polystyrene spheres	$n_{sphere} = 1.5872$	$n_{water} = 1.332$	see Suppl. table 2	see Suppl. table 2	see Suppl. table 2	see Suppl. table 2

^a Calculated using Mie and Percus-Yevick theory [23]. ^b Anisotropy (g) is the average cosine of the scattering angle. ^c See ref [18]. ^d Calculated for an equivolumetric sphere with the same volume as an human/chick RBC [18,20] ^e See ref [21] ^f See ref [24].

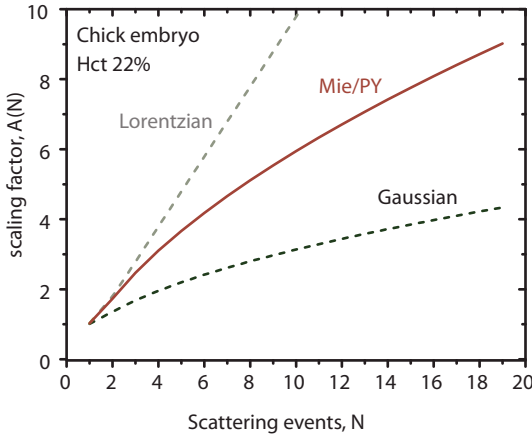
 Table S4.2. Optical properties of polystyrene sphere solutions in water at 632.8 nm^a

Size series			Volume fraction series								
2.5 vol%			1 μm			2 μm			5 μm		
D^b	μ_s^c	g^d	vol%	μ_s^c	g^d	vol%	μ_s^c	g^d	vol%	μ_s^c	g^d
0.6	63	0.848	0.64	24	0.917	1.9	45	0.912	1.1	6.9	0.864
1	89	0.914	0.83	31	0.917	2.5	58	0.911	1.5	9.4	0.864
2	58	0.911	1.2	44	0.916	3.5	80	0.909	2.5	15	0.862
5	15	0.862	2.5	89	0.914	4.4	98	0.908	4.1	25	0.859
7	13	0.918				5.5	120	0.906	6.9	40	0.854
10	7.5	0.899				6.9	147	0.903			

^a Calculated using Mie and Percus-Yevick theory [23]. ^b D is diameter in μm . ^c μ_s in mm^{-1} .

^d Anisotropy (g) is the average cosine of the scattering angle.

S4.6 MULTIPLE SCATTERING SCALING FACTOR FOR CHICK EMBRYO BLOOD



Supplementary Figure S4.5 | Multiple scattering scaling factor for α , $A(N)$ for chick embryo blood. $A(N)$ is plotted versus multiple scattering events, N , in chick embryo blood calculated using our model based on Mie/PY scattering (red line). Dashed lines represent A , for Lorentzian (grey) and Gaussian (black) models for g_1 . All scaling factors are calculated using a normal distribution for $p(n)$ for Hct = 22%.

S4.7 MICROCIRCULATORY FLOW MAPPING

With conventional-SDF and SDF-LSCI images at multiple exposure times at hand, a quantitative blood flow map can be constructed. We applied the following steps:

1. Raw speckle images were converted to K -images by calculating the ratio of standard deviation and mean intensity at each pixel from a local neighbourhood using a spatiotemporal local region of 7×7 (spatial) \times 20 (temporal) pixels.
2. For each pixel in the K -image a multi-exposure curve fit is performed (with a priori estimated β_M and ρ as fixed parameters, as described in Methods and Supplementary Section Id) to estimate $\tau_{c,total}$
3. To correct for offset decorrelation $\tau_{c,offset}$ is estimated as the average of the lowest 10% of pixels in the $1/\tau_{c,total}$ map and τ_c is calculated per pixel according to [10]:

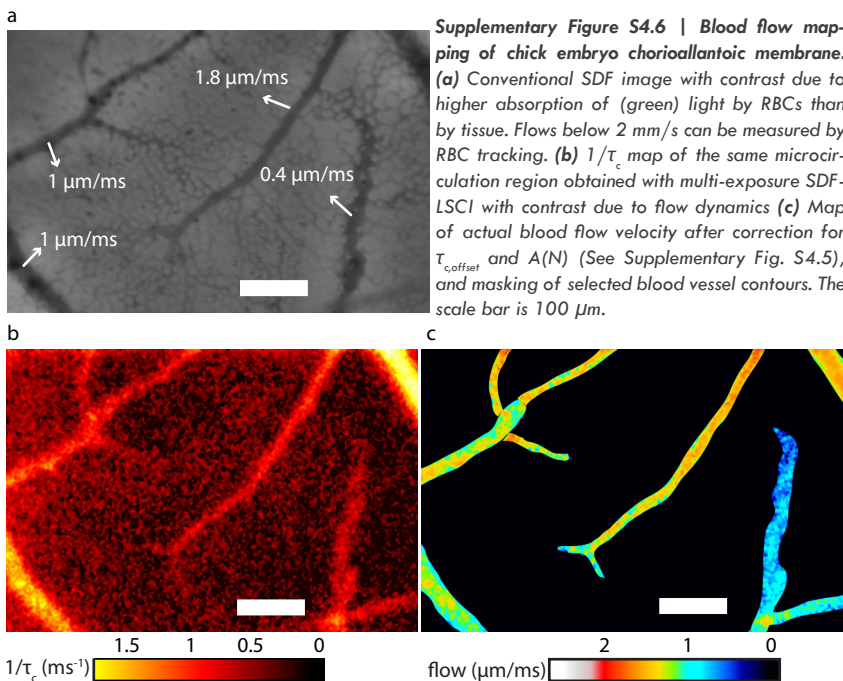
$$\tau_c = \tau_{c,offset} \cdot \tau_{c,total} / \left(\tau_{c,offset}^2 - \tau_{c,total}^2 \right)^{1/2} \tag{4.11}$$

An example of such $1/\tau_c$ map (perfusion map) in false colour is shown in Fig. 4.5b (human, main paper) and Supplementary Fig. 4.6b (chick embryo).

4. For selected vessels the diameter is estimated from the conventional-SDF images and N is estimated following Supplementary Fig. S4.3 based on Monte Carlo simulations of our measurement geometry.
5. Selected vessels are manually masked based on conventional SDF images and $1/\tau_c$ is corrected for multiple scattering according to $1/\tau'_c = (1/\tau_c)/A(N)$, see Fig. 4.6 (human, main Chapter 4) and Supplementary Fig. S4.5 (chick embryo)
6. The resulting map is represented in false colour to visualize the blood flow (Fig. 4.5c, main Chapter 4 and Supplementary Fig. S4.6c), using $1/\tau'_c \approx [0.39 \pm 0.15]V$

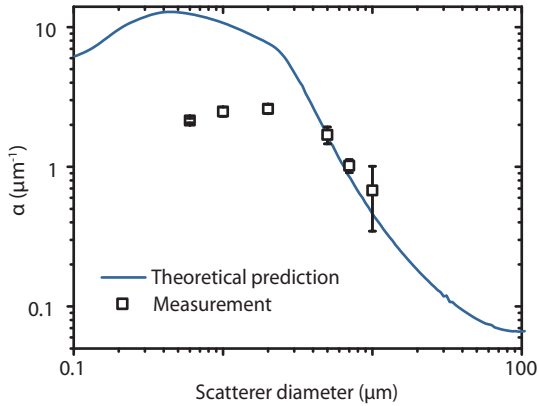
This practical guide shows the feasibility of quantitative flowmetry. We identified the following revisions for enhanced performance. Step 3: The offset decorrelation correction would be improved if a site adjacent to each vessel is selected to estimate $\tau_{c,offset}$. Step 4: The vessel diameter can vary along a vessel and at intersections, therefore an improved estimate of N can be obtained by measuring the diameter dynamically along the vessels. Step 5: Vessel masking is done manually for selected vessels, automatic masking will be more complete and efficient.

In Supplementary Movie 2[§] a video representation of Supplementary Fig. S4.6 is shown for the chick embryo microcirculation.



[§] Movie 2 can be downloaded at

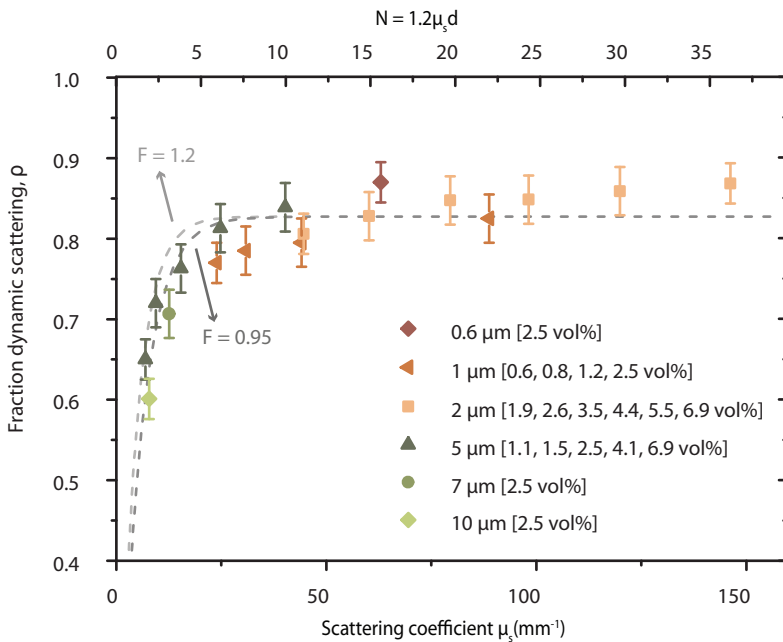
<https://www.dropbox.com/s/kl1ctnxxtraakbw/Movie%20%20Chick%20embryo.avi?dl=0>

S4.8 THEORETICAL PREDICTION FOR α VERSUS SCATTERER DIAMETER (POLYSTYRENE SPHERES)

Supplementary Figure S4.7 | α versus size. Measurement and theoretical prediction for α versus scatterer diameter (polystyrene spheres) in logarithmic scale showing the saturation of α for small diameters. Error bars are 95% CI intervals. Theoretical α is derived using Mie-Percus-Yevick scattering approximations and the number of scattering events N as obtained from Monte Carlo simulations ($N = 1.2\mu_d$) for the *in vitro* flow phantom set-up.

S4.9 EXPERIMENTAL VALIDATION OF MONTE CARLO SIMULATIONS

The number of scattering events N in the tube (phantom experiment) was estimated with Monte Carlo simulations (Supplementary Section 4.3), and yielded: $N = F\mu_s d$, with $F = 1.2$. We validate this estimation using experimental values of ρ (the fraction of detected photons that have been dynamically scattered). The probability of photons reaching the vessel is denoted c_1 . The probability of crossing the vessel with path length l without scattering events follows from Beer's law as $\exp(-\mu_s l)$, where μ_s is the scattering coefficient. Normalizing the path length on vessel diameter d using $l = F \cdot d$ we obtain the probability for passing the vessel under the condition of one or more scattering events as $[1 - \exp(-\mu_s F \cdot d)]$ so that ρ can be estimated as $\rho = c_1 [1 - \exp(-\mu_s F \cdot d)]$. In Supplementary Fig. S4.8 ρ is plotted for all *in vitro* measurements. The best fit yielded $c_1 = 0.83$ and $F = 0.95$ [95% upper CI - lower CI: 0.81 - 1.1], $r^2 = 0.83$. Fixing $F = 1.2$ to match the Monte Carlo estimation resulted in $r^2 = 0.74$. Both fits are plotted in Supplementary Fig. S4.8 and resemble the data. This analysis confirms our simulated estimate for N .



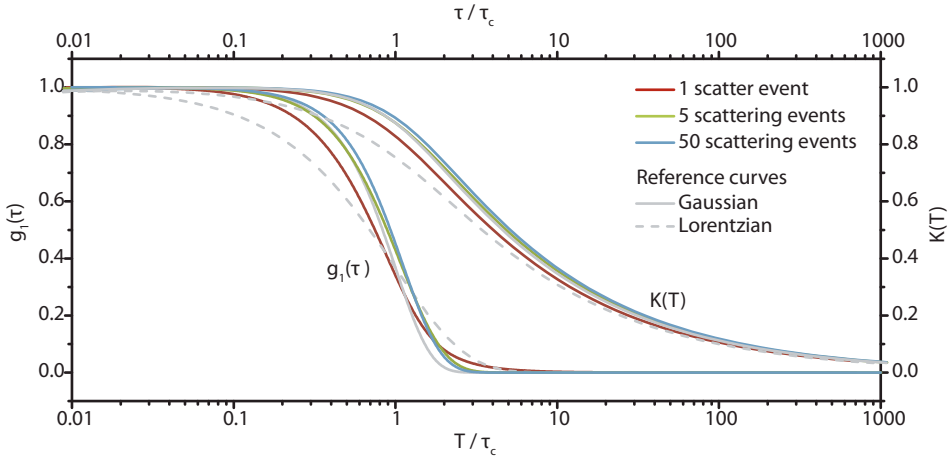
Supplementary Figure S4.8 | Fraction dynamically scattered light (ρ) versus scattering properties. The dashed line represents a curve fit (see text above) of $\rho = c_1 [1 - \exp(-\mu_s F \cdot d)]$ with fit parameters $c_1 = 0.83$ and $F = 0.95$ ($r^2 = 0.83$), or $F = 1.2$ ($r^2 = 0.74$)

S4.10 INFLUENCE OF GAUSSIAN APPROXIMATION ON $K(T)$

The decorrelation time τ_c is derived from the measurement of spatial speckle contrast K vs. integration time T by fitting an analytical model to the measurements. The model in Supplementary equation (4.10) assumes a Gaussian form of the autocorrelation function $g_1(\tau)$ which we justify by the approximately Gaussian form of all distributions in the model:

- The velocity distribution $P(V)$ is assumed to Gaussian because of the randomization of the scattering vector \mathbf{q} with respect to the flow velocity vector \mathbf{V} . This assumption is not expected to hold all experimental geometries; e.g. for collimated incident light on a laminar flow profile.
- The phase function $p(\mathbf{q})$ is approximately Gaussian for particles with little refractive index difference from their suspended medium. For large particles with high refractive index contrast this assumption has limited accuracy.
- The distribution of the number of scattering events is Poissonian for highly diluted samples. We assume a Gaussian distribution of n which will be less valid for small number of scattering events.

We calculated $g_1(\tau)$ and $K(T)$ using our model for RBCs, and $N = 1, 5$ and 50 scattering events, respectively, yielding $\tau_c(1)=2.66$ ms; $\tau_c(5)=0.78$ ms and $\tau_c(50)=0.18$ ms. Supplementary Fig. S4.9 shows both groups of curves simulated for a flow velocity $V = 1 \mu\text{m}/\text{ms}$. We then calculate $g_1(\tau)$ and $K(T)$ for the Gaussian ACF using the respective values for τ_c (Supplementary equation (4.7)). Subsequent scaling of the time-axes on τ_c causes these latter curves to overlap. For reference, $g_1(\tau)$ and $K(T)$ based on the Lorentzian model (appropriate when Brownian motion is considered) are also provided. From the close resemblance of $K(T)$ curves using our model of $g_1(\tau)$ and that obtained from a Gaussian form with the same τ_c , we conclude that τ_c can be retrieved adequately using Supplementary equation (4.10). We note that this result does not imply that $g_{1,\text{single}}(\tau)$ is Gaussian nor that the scaling factor based on this assumption should be used ($A(N) \sim \sqrt{N}$, reference curve in Supplementary Fig. S4.5 and main Chapter Fig. 4.6). Rather, the $K(T)$ curve at any number of scattering events can be fitted with Supplementary Eq. (4.10) to yield τ_c and model based rescaling to τ'_c follows from the Mie/PY curve in Supplementary Fig. S4.5 and main Chapter Fig. 4.6.



Supplementary Figure S4.9 | Theoretical modelling of $g_1(\tau)$ and $K(T)$ in the multiple scattering regime. $g_1(\tau)$ and $K(T)$ are theoretically calculated for the optical and geometrical properties of RBCs, for $N = 1$ (red), 5 (green) and 50 (blue) scattering events, yielding $\tau_c = 2.66$ ms, $\tau_c = 0.78$ ms and $\tau_c = 0.18$ ms for $N = 1, 5, 50$ respectively. Gaussian (solid line) and Lorentzian (dashed line) models with the same τ_c are also plotted. A flow velocity of $V = 1$ $\mu\text{m}/\text{ms}$ was used in the calculation.

S4.1.1 RELATION TO DIFFUSING WAVE SPECTROSCOPY AND LASER DOPPLER FLOWMETRY

The model presented in Supplementary Section 4.1 is of similar form and origin as the theory for Diffusive Wave Spectroscopy (DWS) [23, 24] and for Laser Doppler flowmetry (LDF) [6]. Our model differs in two key areas with both. The first area covers the different approaches in deriving the ACF for single scattering events $g_{1,\text{single}}$. Rather than carrying out the integration over the velocity distribution, leading from Supplementary Eq. (4.2) to Supplementary Eq. (4.3), DWS uses a cumulant expansion for short times τ to bring the ensemble average into the exponential:

$$g_{1,\text{single}}(\tau) = \begin{cases} \left\langle \exp\left(-q^2 V^2 \tau^2 / 6\right) \right\rangle_q & \text{This work, Supplementary equation (4)} \\ \exp\left(-\langle q^2 \rangle_q V^2 \tau^2 / 6\right) & \text{Diffusive Wave Spectroscopy, ref [21]} \end{cases} \quad (4.12)$$

Where the $\langle \dots \rangle_q$ represents integration over the phase function. For DWS, $\langle q^2 \rangle_q$ evaluates to $2k_0^2(1-g)$ where g is the average cosine of the scattering angle. Then, the scaling factor a' between the inverse of the decorrelation time and flow velocity, $1/\tau_c = a'V$ becomes:

$$\alpha'_{DWS} = k_0 \sqrt{\frac{1}{3}(1-g)} \quad (4.13)$$

4

We note that the dependence on particle diameter and volume fraction is included in g . Using Supplementary Table S4.1 we find $\alpha'_{DWS} \approx 0.54$ in the human microcirculation. The LDF framework proceeds to integrate Supplementary Eq. (4.12) over \mathbf{q} , weighted by the form factor, which is equivalent to our weighting with the phase function. However, LDF uses the Rayleigh-Gans (RG) approximation to estimate the angular distribution of scattered light, whereas we use the more generically applicable Mie theory combined with Percus-Yevick equation to account for volume fraction effects. LDF [6] proceeds to approximate the RG phase function by a Gaussian form leading to

$$\alpha'_{LDF} \approx \frac{1}{1.35r} \quad (4.14)$$

Where r is the particle radius. Our definition of τ_c in Supplementary Eq. (4.7) differs from the definition by Bonner and Nossal [6] who use $\tau_{1/2}$, which is related to τ_c by $\tau_{1/2} = \tau_c \sqrt{4 \ln 2 / \pi}$. For comparison reasons we adhere to our definition which explains the difference of the factor 1.35 with the factor 1.27 that is often cited in literature. For human blood we find $\alpha'_{LDF} \approx 0.26$.

The second key difference concerns how multiple scattering is treated. Our summation over the number of scattering events n is replaced by integration over the path length distribution $p(l)$. The two quantities are related through $l = n/\mu_s$:

$$g_1(\tau) = \begin{cases} \sum_n p(n) \left\langle \exp(-n\mathbf{q}^2 V^2 \tau^2 / \delta) \right\rangle_{\mathbf{q}} & \text{This work, Supplementary equation (5)} \\ \int p(l) \exp(-2k_0^2(1-g)V^2 \tau^2 l / \delta) & \text{Diffusive Wave Spectroscopy, ref [21]} \end{cases} \quad (4.15)$$

Expressions for $p(l)$ can then be derived from e.g. the radiative transport equation [24], or, similar to our approach, approximated from Monte Carlo simulations [25]. LDF assumes the Poissonian form of $p(n)$ to carry out the summation, thereby essentially limiting the range of validity to low volume fractions. Contrary to the coherent techniques discussed here, low coherence interferometry allows control over $p(l)$, either coercing the experiment to single scattering [26] or low-order scattering [27]. The latter work proposes an empirical correction to the assumed Poissonian form of $p(l)$. Part of the correction is related to instrumental factors, part is attributed to volume fraction-dependent effects on the optical properties (correctly so in our opinion for the reasons given in Supplementary section 4.1 c). The choice of $p(n)$ becomes of lesser influence as the mean number of scattering events N increases, because all forms of $p(n)$ eventually become Gaussian as per the Central Limit Theorem.

S4.12 REFERENCES FOR SUPPLEMENTARY INFORMATION TO CHAPTER 4

1. H. C. Hulst, *Light scattering by small particles* (Courier Dover Publications, 1957).
2. J. K. Percus and G. J. Yevick, "Analysis of classical statistical mechanics by means of collective coordinates," *Physical Review* **110**, 1 (1958).
3. M. Wertheim, "Exact solution of the Percus-Yevick integral equation for hard spheres," *Phys. Rev. Lett.* **10**, 321-323 (1963).
4. B. J. Berne and R. Pecora, *Dynamic light scattering: with applications to chemistry, biology, and physics* (Courier Dover Publications, 2000).
5. D. Boas and A. Yodh, "Spatially varying dynamical properties of turbid media probed with diffusing temporal light correlation," *JOSA A* **14**, 192-215 (1997).
6. R. Bonner and R. Nossal, "Model for laser Doppler measurements of blood flow in tissue," *Applied optics* **20**, 2097-2107 (1981).
7. J. W. Goodman, *Speckle phenomena in optics: theory and applications* (Roberts and Company Publishers, Greenwood Village, CO, 2007).
8. J.-P. Hansen and I. R. McDonald, *Theory of simple liquids* (Elsevier, Amsterdam, 1990).
9. L. Tsang, J. A. Kong, and K.-H. Ding, *Scattering of Electromagnetic Waves, Theories and Applications* (John Wiley & Sons, New York, 2004), Vol. 27.
10. A. Nadort, R. G. Woolhuis, T. G. van Leeuwen, and D. J. Faber, "Quantitative laser speckle flowmetry of the *in vivo* microcirculation using sidestream dark field microscopy," *Biomedical optics express* **4**, 2347-2361 (2013).
11. D. A. Boas and A. K. Dunn, "Laser speckle contrast imaging in biomedical optics," *Journal of biomedical optics* **15**(2010).
12. A. B. Parthasarathy, W. J. Tom, A. Gopal, X. Zhang, and A. K. Dunn, "Robust flow measurement with multi-exposure speckle imaging," *Opt. Express* **16**, 1975-1989 (2008).
13. P. Zakharov, A. Völker, A. Buck, B. Weber, and F. Scheffold, "Quantitative modeling of laser speckle imaging," *Opt. Lett.* **31**, 3465-3467 (2006).
14. D. D. Duncan and S. J. Kirkpatrick, "Can laser speckle flowmetry be made a quantitative tool?," *JOSA A* **25**, 2088-2094 (2008).
15. A. B. Parthasarathy, S. Kazmi, and A. K. Dunn, "Quantitative imaging of ischemic stroke through thinned skull in mice with Multi Exposure Speckle Imaging," *Biomedical optics express* **1**, 246-259 (2010).
16. F. F. M. de Mul, "Monte-Carlo simulation of Light transport in Turbid Media," in *Handbook of Coherent Domain Optical Methods, Biomedical Diagnostics, Environment and Material Science*, V. V. Tuchin, ed. (Kluwer Publishers, 2004), pp. 465-533.
17. F. F. M. de Mul, M. H. Koelink, M. L. Kok, P. J. Harmsma, J. Greve, R. Graaff, and J. G. Aarnoudse, "Laser Doppler velocimetry and Monte Carlo simulations on models for blood perfusion in tissue," *Appl. Opt.* **34** (1995).
18. N. Bosschaart, G. J. Edelman, M. C. Aalders, T. G. van Leeuwen, and D. J. Faber, "A literature review and novel theoretical approach on the optical properties of whole blood," *Lasers Med. Sci.* **29**, 453-479 (2014).
19. A. R. Pries, T. W. Secomb, P. Gaetgens, and J. Gross, "Blood flow in microvascular networks. Experiments and simulation," *Circ. Res.* **67**, 826-834 (1990).
20. L. Chan, "Changes in the composition of plasma membrane proteins during differentiation of embryonic chick erythroid cell," *Proceedings of the National Academy of Sciences* **74**, 1062-1066 (1977).
21. P. M. Johnston, *Hematocrit Values for the Chick Embryo at Various Ages* (1955), Vol. 180, pp. 361-362.
22. A. Nicolet and F. Meli, "Report on the needs, specifications and commercial sources of microvesicle reference materials," (EMRP JRP HLT02 MetVes, 2012).
23. D. Pine, D. Weitz, P. Chaikin, and E. Herbolzheimer, "Diffusing wave spectroscopy," *Phys. Rev. Lett.* **60**, 1134 (1988).
24. D. Weitz, J. Zhu, D. Durian, H. Gang, and D. Pine, "Diffusing-wave spectroscopy: The technique and some applications," *Phys. Scr.* **1993**, 610 (1993).
25. T. B. Rice, E. Kwan, C. K. Hayakawa, A. J. Durkin, B. Choi, and B. J. Tromberg, "Quantitative, depth-resolved determination of particle motion using multi-exposure, spatial frequency domain laser speckle imaging," *Biomedical optics express* **4**, 2880-2892 (2013).
26. J. Kalkman, R. Sprik, and T. van Leeuwen, "Path-length-resolved diffusive particle dynamics in spectral-domain optical coherence tomography," *Phys. Rev. Lett.* **105**, 198302 (2010).
27. A. Wax, C. Yang, R. R. Dasari, and M. S. Feld, "Path-length-resolved dynamic light scattering: modeling the transition from single to diffusive scattering," *Appl. Opt.* **40**, 4222-4227 (2001).